# Chemical and physical effects of high-volume limestone powder on sodium silicate-activated slag cement (AASC)

Xiaohong ZHU[a,b], **Kai YANG**[a,b]*, Shouheng JIANG[c], Changhui YANG[a].

a. College of Materials Science and Engineering, Chongqing University, 400045, China
b. School of Civil Engineering, University of Leeds, LS2 9JT, UK
c. School of Technology, Harbin University, 150086, China

* Corresponding author: yang.kai@cqu.edu.cn

## Abstract

This study aims at discussing physical and chemical influence of limestone powder (LS) on the AAS system. General properties, including fluidity, setting time, drying shrinkage, and mechanical strength of AAS pastes/mortars, were examined. Pore structure change and phase assemblages of LS-AAS composites were studied. The results showed that the addition of 50 wt. % LS increased the fluidity and setting time of AAS pastes, but reduced the total drying shrinkage of AAS mortars. Meanwhile, around 30% reduction in mechanical properties were found at the same replacement ratio. The pore structure was refined in the pastes with LS replacement less than 25 wt. %, but was coarsened in the sample with 40 wt. % LS. Limited new phase was formed in the sodium silicate activated slag samples, which was believed to depend on the modulus of the activator. Around 30% hydration degree of LS was achieved in 40 wt.% LS-replaced AAS pastes hydrated for 7~28 d as determined by TG-DSC analysis. The main drawbacks of AAS, fluidity, setting time, and drying shrinkage, are improved by using high-volume LS, so use of high-volume LS in AAS system can be an option for the purpose of environmental protection.

**Keywords:** alkali-activated slag cement, limestone powder, microstructure, shrinkage

## 1. Introduction and research motivation

The climate problem forces the cement industry, which accounts for ~ 5-8 % total anthropogenic $CO_2$ emissions [1], to seek for alternative binders to reduce the carbon footprint [2]. The alkali-activated slag cement (AASC) show promising performance even when involving high-volume fillers with lower activity [3]. The binder of AASC is not only limited to granulated blast furnace slag (GGBS), but also includes other precursors e.g. fly ash or metakaolin to adjust the matrix properties [4]. Within all alternative precursors in the AASC system, limestone powder (LS) is believed to be an attractive component, as it is widely available, abundant, cheap and with no requirements of thermal treatment [5]. Ortega-Zavala et al [5] recently tried to use the limestone powder as the sole binder to prepare the sodium silicate (Ms=1.0 and 1.5) activated pastes, which gave 15~25 MPa after 1 year. The $^{29}$Si MASNMR indicated that the main binding phase, C-S-H gel, was formed in such a system [5]. These results are encouraging that directly proved the limestone is active when sodium silicate is present in the system, which provides the theoretical basis for the use of LS in sodium-silicate-based AASC system.

Limestone powder has been used as either 'inert filler' or supplementary cementitious materials in multiple systems for a long time [6]. In cement-based materials, the LS powder mainly affect the matrix's properties by filler, nucleation, dilution and chemical effects [6]. In slag-concrete, the addition of LS can improve the early-strength and workability of the mixtures, which could make 60% reduction in CO2 emission by combined using LS and slag [7]. This combination could also achieve around 20% reduction in concrete production cost according to Li's estimation [7]. The LS will be more active if the alkali (CaO or NaOH) is present [8], which will change the molecular structure of the original silica-gel that formed in alkali-activated waste glass matrix, further improved the hydraulic and mechanical properties of the matrix. For the NaOH activated natural pozzolan/LS mortar, the increase of alkali concentration will enhance the pore-filling effect, calcium reactivity and density of the final hardened matrix [9], in which, the supplementary Ca-source provided by LS is critical. Xiang [10] systematically studied the effect of LS on the properties of alkali-activated fly ash/slag samples, who found that the low dosage (< 20%) LS could improve the rheological and mechanical properties of the matrix, and also reduce the drying shrinkage of hardened mortars. However, Yuan [11] found that the autogenous shrinkage of sodium carbonate activated slag increased when included low dosage (< 30%) LS but decreased when higher content LS was added. The above studies showed the potential application of LS in cement-based materials, especially the alkali-activated materials, which provide the basis for the current study.

**Figure 1** provides estimates of embodied carbon emission from the consumption of whole process of construction

based on the Inventory of Carbon and Energy (ICE) database (https://circularecology.com/). The PC-concrete that based on CEMI is used as the reference and the activator content for AASC is selected as 5 wt. % of the total binder (LS+GGBS). With the consideration of production, transportation, concrete batching, and casting, approximately 420 kg $CO_2$eq will be generated per cubic concrete. However, ~ 70% $CO_2$eq is reduced by using pure AAS concrete. Although, the replacement of supplementary cementitious materials in CEMI will reduce up to 30 ~ 40 wt.% $CO_2$ emissions without suffering significant changes in performance [12], the AAS concrete still shows approximately 40% less $CO_2$eq emission. The use of LS to replace the GGBS in AASC will further reduce the carbon emissions of concrete, especially at high volume replacement ratio. In addition, the LS occupies ~ 15% of the earth crust, which is an easier accessible materials that need to be fully used [5].

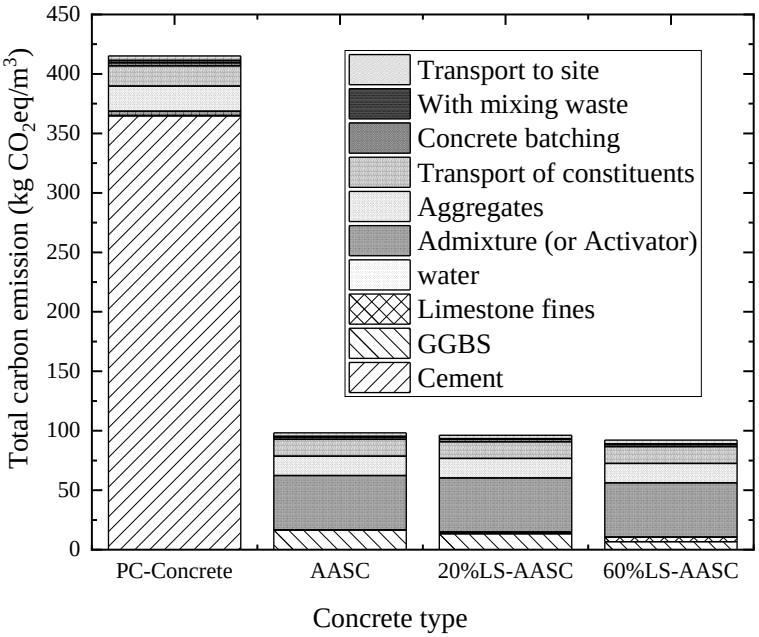


**Figure 1.** Estimation of Embodied Carbon Footprint of CEMI-concrete (PC-concrete), AAS concrete and LS-powder modified AASC based on the Inventory of Carbon and Energy (ICE) database (https://circularecology.com/).

The current study aims at using high-volume of LS (up to 50 wt.%) to replace the GGBS in AASC. To achieve this, the general properties (fluidity, setting time, and mechanical properties) and drying shrinkage (one of the main drawbacks of AASC [3]) of the obtained mixtures or hardened matrixes. Microstructural analysis, including pore structure, phase assemblage, and morphology are examined through $N_2$-adsorption test, XRD, FTIR, and SEM-EDX techniques. These microstructural changes support the macro-properties performance and provide a clear understanding of the behaviours of LS in AASC system.

# 2. Experimental details

## 2.1 Raw materials

The granulated blast furnace slag (GGBS) was provided by Chongqing Iron & Steel Company (Changshou, Chongqing), which was dried and ground in a ball mill for 35 min. The specific area and density of the GGBS were 350 $m^2$/kg (Blaine fineness) and 2.85 g/$cm^3$ respectively according to GB/T8074-2008. The chemical composition (**Table 1**) is determined according to Chinese standard GB/T 18046-2008 using chemical methods as explained in our previous paper [13]. The commercial limestone powder (LS) was provided by Bao Xing Company (Sichuan) and the mineralogy information (XRD pattern) was given in the study of Luo et al [14]. The specific surface area of LS was 400 $m^2$/kg and the chemical composition is also given in **Table 1**. Both particle size distribution of LS and GGBS were measured by Mastersizer APA2000 (Malvern Panalytical, UK) and given in **Figure 2**. Clearly, the LS is slightly finer than GGBS as shown by specific surface area and particle size distribution.

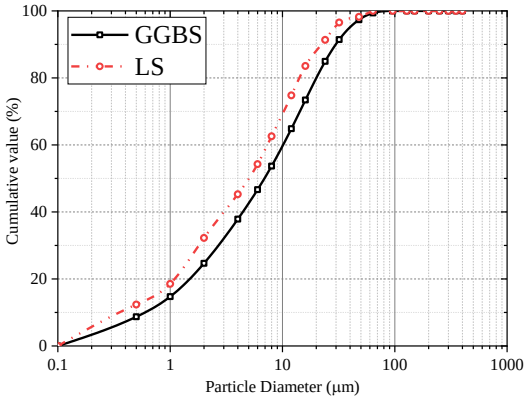


**Figure 2** Particle size distribution of GGBS and LS powders.

**Table 1** Chemical composition of GGBS and LS (%)

| Composition | $SiO_2$ | $Al_2O_3$ | $Fe_2O_3$ | MgO | CaO | $Na_2O$ | $K_2O$ | LOI |
|---|---|---|---|---|---|---|---|---|
| GGBS | 32.61 | 14.44 | 1.03 | 9.39 | 36.18 | 0.40 | 0.42 | 0.57 |
| LS | 0.23 | - | 0.21 | - | 55.46 | - | - | 41.75 |

## 2.2 Sample preparation

Commercial sodium silicate solution (water glass, Chongqing Jingkou Chemical Plant) with an initial modulus (Ms) of 2.50 was used. It was composed of 29.07 wt.% $SiO_2$, 12.02 wt.% $Na_2O$, and 53.80 wt.% $H_2O$. NaOH pellet (Xinjiang Tianye Chemical Plant) was added to adjust the Ms of water glass into 1.20. The NaOH solution (50 wt.%) was prepared and cooled in a sealed plastic beaker, then gradually added into sodium silicate solution accompanied by stirring. The obtained activator was sealed and cooled to room temperature. The water in the activator was included in the water/binder (w/b) ratio for all pastes (w/b=0.35) or mortars (w/b=0.40).

Mortars that used for mechanical properties and drying shrinkage tests were prepared according to the mix proportion given in **Table 2**. The LS gradually replaced GGBS from 0 wt.% to 50 wt.% with an interval of 5 wt.%. The activator was 5 wt. % ($Na_2O$eq) of the binder content (GGBS+LS). Before adding the activator, the powders were mixed for 60 s and then the sand was gradually added into the mixed powders for another 120 s in a planetary mixer. The activator was then slowly added into the mixture for another 120 s mixing. The mortars that used for compressive/flexural strength and drying shrinkage were cast into the 40 mm × 40 mm × 160 mm moulds in two layers and vibrated to eliminate the voids on a vibration table. The samples were then covered with plastic film to avoid moisture loss and then de-moulded after initial 24 h curing.

AAS pastes that used for fluidity, setting time, and microstructural analysis were prepared separately with a consistent w/b ratio of 0.35. The powders were pre-mixed for 60 s and then the activator was added into the powders in a small planetary mixer for 2-min mixing. The samples that used for microstructural analysis were cast into a small plastic tube and cured in a standard curing room with a temperature of 20 ± 2 °C and a relative humidity (RH) of 100% until testing ages.

**Table 2** Mix proportions of AAS/LS mortars

| Sample | LS (%) | LS (g) | GGBS (g) | Water (g) | Activator (%) | Sand (g) |
|---|---|---|---|---|---|---|
| AAS | 0 | 0 | 500 | 200 | 5 | 1500 |
| 5LS/95AAS | 5% | 25 | 475 | 200 | 5 | 1500 |
| 10LS/90AAS | 10% | 50 | 450 | 200 | 5 | 1500 |
| 15LS/85AAS | 15% | 75 | 425 | 200 | 5 | 1500 |
| 20LS/80AAS | 20% | 100 | 400 | 200 | 5 | 1500 |
| 25LS/75AAS | 25% | 125 | 375 | 200 | 5 | 1500 |
| 30LS/70AAS | 30% | 150 | 350 | 200 | 5 | 1500 |
| 35LS/65AAS | 35% | 175 | 325 | 200 | 5 | 1500 |
| 40LS/60AAS | 40% | 200 | 300 | 200 | 5 | 1500 |
| 45LS/55AAS | 45% | 225 | 275 | 200 | 5 | 1500 |
| 50LS/50AAS | 50% | 250 | 250 | 200 | 5 | 1500 |

## 2.3 Testing methods

The test methods were grouped according to the type of specimen, which are shown below:

**1) AAS pastes:** The fluidity was carried out by mini-slump test (36 mm × 60 mm × 60 mm cone mould) according to Chinese standard GB/T 8077-2012. The average of 4 orthogonal directions were recorded as the fluidity (the accuracy of readings is 5 mm, which is given as the error bar of the reported values). The setting time were measured using a Vicat apparatus according to GB/T 1346-2011.

Meanwhile, to examine the microstructure, the hardened AAS pastes were initially crushed into small pieces with a diameter of 4-5 mm. The crushed samples were hydration-stopped using solvent-exchange method [13, 15] and dried in a vacuum oven at 40 $^{o}$C. The crushed sample were then characterised by SEM-EDX (gold-coated; Zeiss Auriga FIB/SEM operated at 30kV, with the magnifications of 5.0k and 10.0k) and $N_2$-adsorption test (Micrometrics ASAP 2020 Automated Surface Area and Porosimetry System at a constant temperature of 77.350 K). The specific surface area was calculated with the Brunauer-Emmett-Teller (BET) equation, and the pore size distributions were calculated from the adsorption curve by the Barrett-Joyner-Halenda (BJH) method. The crushed samples were then ground into fine powder and followed by characterising with X-ray diffraction (XRD, PIGAKV D/Max-5A12kW operated with Cu Kα radiation (λ=1.54 Å) with a scanning rate of 4°/min), FTIR (Nicolet iS5; 64 scans with resolution of 4 $cm^{-1}$), and TG-DSC (Netzsch STA 250; from room temperature to 1000 $^{o}$C; 20 $^{o}$C/min; $N_2$ atmosphere). The details of quantifying the contents of calcium hydroxide and calcium carbonates are discussed in Section 3.3.3 in joint with the TG-DSC data of raw limestone powder.

**2) AAS mortars:** The mechanical properties of AAS mortars were determined in accordance to Chinese standard GB/T 17671-1999 at 3 d, 7 d, 28 d, and 56 d. The reported flexural strength value is a mean value of 3 samples and that for compress strength is a mean value of 6 samples. Drying shrinkage was measured using a length comparator to determine the linear length change of prism samples according to the method given in Jin et al. [16]. The shrinkage was tested under a temperature of 20 ± 2 $^{o}$C and a relative humidity (RH) of 60 ± 5 %.

# 3. Results and discussion

## 3.1 General properties

**Figure 3** shows the general properties of AAS/LS composites with the LS replacement ratio gradually changed from 0 wt.% to 50 wt.%. Both fluidity (**Figure 3a**) and initial setting time (**Figure 3b**) of AAS/LS pastes increase with the loading of LS, which will be better for the 'handling period' for AAS concrete. This result agrees the behaviour of LS in thermally-activated halloysite [17]. Even through, the increase of setting time is far less than that needed for practical use, the retarder is still needed for AAS. The fluidity and setting of AAS pastes depend on the formation of the C-S-H skeleton, which requires a certain level of $Ca^{2+}$ concentration in the aqueous phase from the thermodynamic point of view [18]. The Ca-dissolving process of LS in alkaline solution is very slow [5] when compared to that of GGBS, therefore, the Ca concentration is further linked with the GGBS content in the solution. The initial less available $Ca^{2+}$ ions in aqueous phase is responsible for the better fluidity and longer setting time.

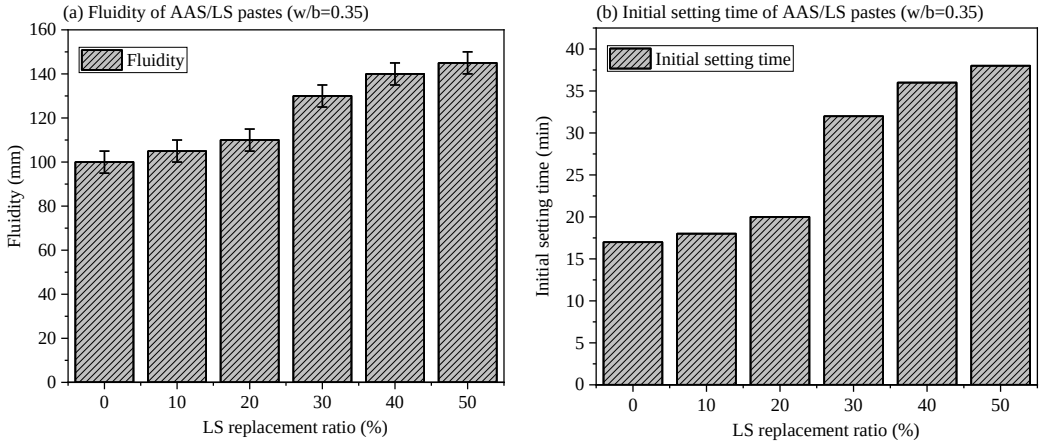

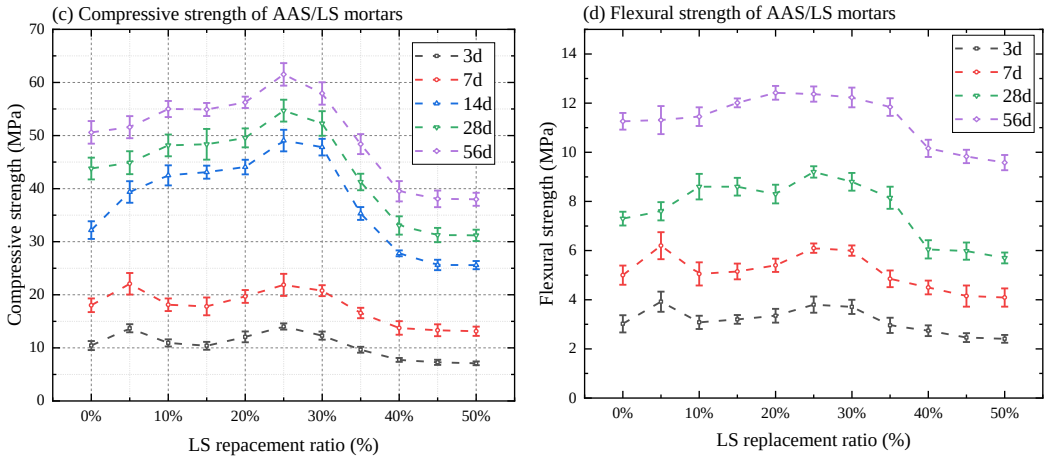


**Figure 3** General properties of AAS/LS composites: (a)-(b) Fluidity and initial setting time of AAS/LS pastes (w/b=0.35) and (c)-(d) Compressive and flexural strengths of AAS/LS mortars (w/b=0.4, sand: binder ratio=3:1).

**Figure 3c and 3d** plot the mechanical strength variations up to 56 d of AAS/LS mortars. As expected, the mortars exhibited a rapid increase of compressive strength until 28 d and a slow increase up to 56 d. Unlike compressive strength, the flexural strength continuously showed a comparable increase rate between 28 d and 56 d when compared to the early age. Nevertheless, the development trend of both compressive and flexural strengths is the same as the increased loading of LS. It showed an increasing trend up to 25 wt. % LS replacement and then a slight decreasing trend until 50 wt. % replacement at each testing age. This trend agrees that in sodium hydroxide-activated metakaolin-based geopolymers [19] and that in alkali waste-activated slag cement systems [20]. It is interesting that the development trend of mechanical properties in AAS/LS composites is the same regardless of LS type but is closely related to the specific surface area of LS [20]. This phenomenon indicates that the initial strength increase should be attributed to the 'filler effect' [6, 21]. The replacement of 50 wt. % LS resulted in 33.88% reduction in compressive strength and 25.66% reduction in flexural strength.

## 3.2 Drying shrinkage and simultaneously mass loss

The drying shrinkage is one of the main drawbacks of the field application of AASC, which was tried to be migrated by using multiple additives such like calcium hydroxide [13], reactive MgO [16], and sulphate-enrichment [22]. Other techniques such like high-temperature curing [22] and internal curing [23] can be used together to minimize the shrinkage of hardened AAS composites. This important property of concern is also measured in AAS/LS mortars and plotted in **Figure 4**.

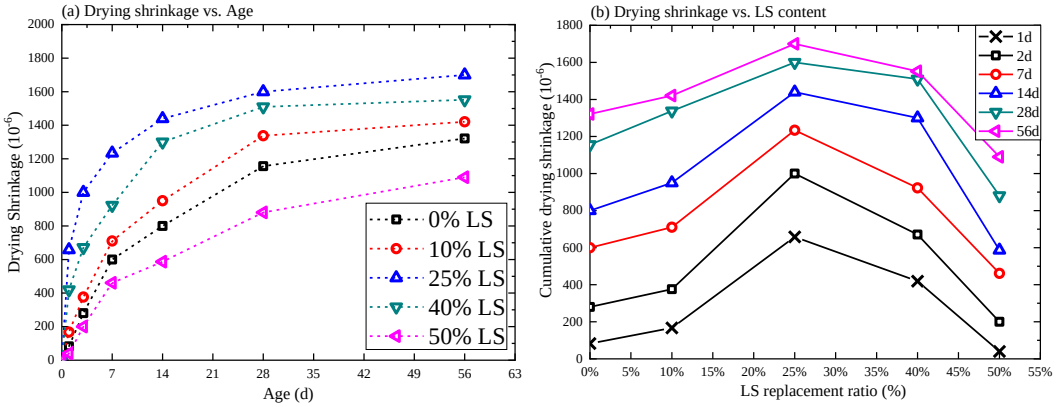

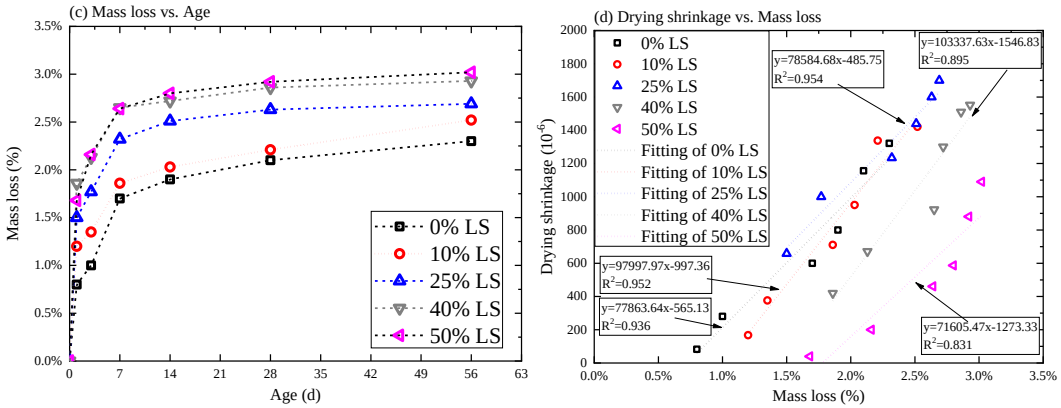


**Figure 4 (a)** Drying shrinkage changes with age; (b) Cumulative drying shrinkage changes with LS replacement ratio and (c) simultaneously mass loss of AAS/LS composites (d) mass loss vs. shrinkage.

**Figure 4a and 4b** show the drying shrinkage of AAS/LS mortars against age and LS replacement ratio respectively. Like the previous studies [15,16,24], most of the shrinkage happened before 28 d and then plateaued afterwards in all groups. As shown clearer in **Figure 4b**, the variation tendency of drying shrinkage is similar to that of mechanical strengths, where the shrinkage increased to highest value at the LS replacement ratio of 25 wt.% and then gradually decreased afterwards. The drying shrinkage development line (**Figure 4a**) of 50LS/50AAS mortar falls below that of neat AAS mortar. This result is controversial to the drying shrinkage of LS-replaced sodium carbonated-activated slag that reported by Yuan et. al [11], where the drying shrinkage consciously increased even when the LS replacement ratio reached 50 wt. %. However, the mass loss trend of the samples agrees that study [11]. However, the autogenous shrinkage of the high-volume LS replaced samples in that study shows a lower value than that of reference group [11]. On the other hand, this result agrees with another study of shrinkage of LS modified alkali-activated slag/fly ash showed that the drying shrinkage was reduced by adding 5 ~ 20 wt. % [10]. The factors that primarily affect the shrinkage (at the fixed environment) should be: i). The volume of binder content in the hardened samples (i. e. the long-term visco-elastic/visco-plastic deformation of C-N-A-S-H [22]); ii). The pore structure changes of the samples (i. e. the drying results of the capillary pressure that acts as the driving force for shrinkage [22]. The addition of high-volume LS will change both factors: i). The volume of paste will be dramatically reduced since the reaction between LS and activator is slow [5]; ii). The pore volume of paste will increase due to insufficient hydration products that can fill the gaps between these particles and the higher effective w/b ratio will left more pores. Therefore, the reduction of drying shrinkage unsurprisingly occurs in such a system.

Meanwhile, the mass loss continuously increased with the addition of LS as shown in **Figure 4c**, which is due to the higher 'effective' w/b ratio will results more pores, however, if the water left from the pores with larger diameters (that cannot easily form capillary meniscus) will not effectively generate shrinkage [25]. In addition, the elastic modulus of LS powder is much higher than that of C-N-A-S-H gel, which will not easily deform when suffering such capillary forces [13]. The relationships of mass loss and drying shrinkage are further established in **Figure 4d**, which is typically a two-step linear relationship but only the deformation period (one linear line) is given here [26]. The slope of the linear fitting lines indicates the 50LS/50AAS mortars showed a slower increase rate of drying shrinkage when compared to that of reference group.

## 3.3 Microstructural analysis

### 3.3.1 Pore structure analysis

**Figure 5** gives the pore structure changes of LS/AAS pastes at 28 d that determined by $N_2$-adsorption method, which is closely linked with mechanical and shrinkage properties. The cumulative pore volume (**Figure 5b**) of AAS pastes with 10 wt.% and 25 wt.% LS replacement ratios had a smaller pore volume when compared to the neat AAS paste, whilst that of 40LS/60AAS pastes gave a fairly-higher total pore volume. This is also supported by the surface area change of these pastes (**Figure 5c**).The variation of pore volume agrees the mechanical changes of the composites as the higher pore volume will result in the lower compressive or flexural strengths of the matrix [27].

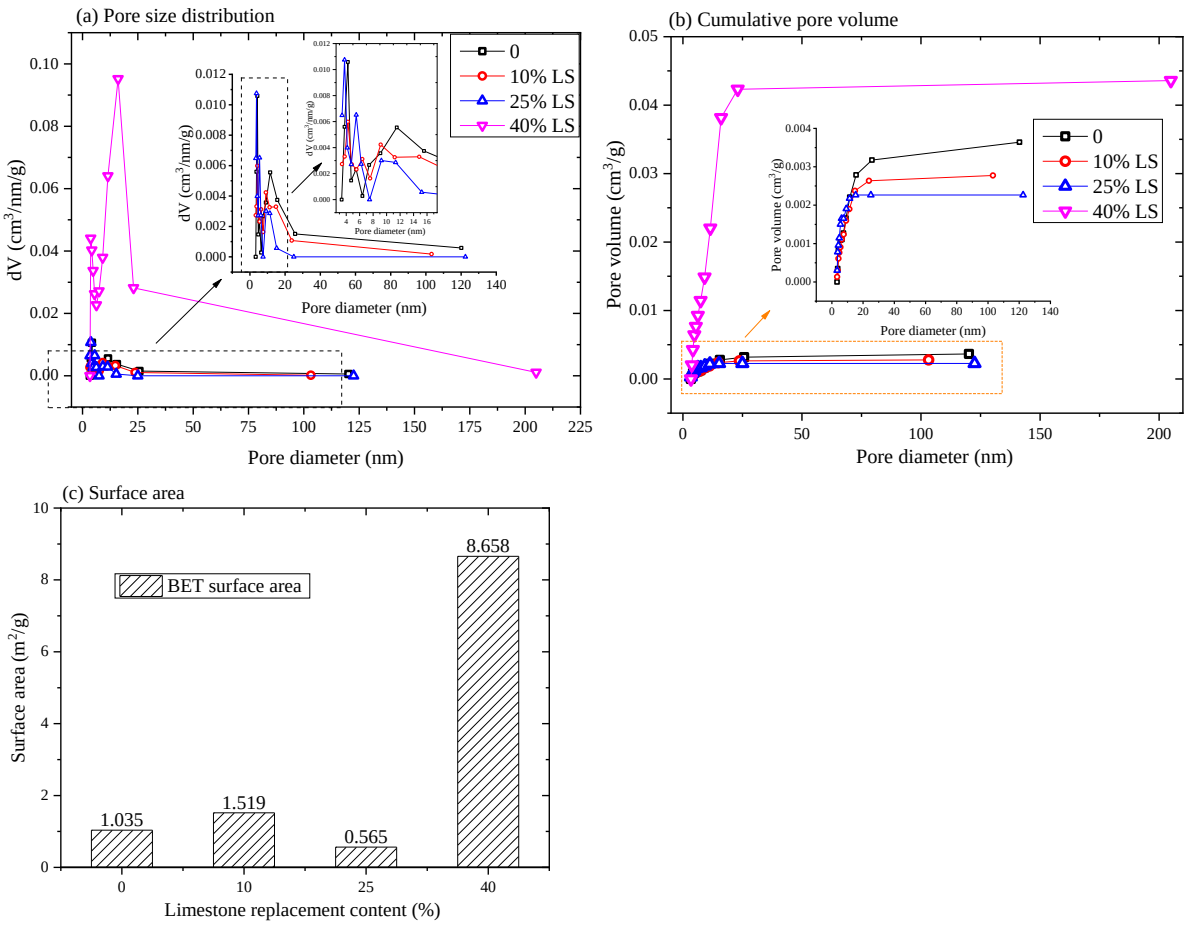


**Figure 5.** Pore structure of AAS/LS composites: (a) pore size distribution; (b) cumulative pore volume; (c) surface area.

It is clearer from the pore size distribution (**Figure 5a**) that the pore structure was refined by the addition of up to 25 wt. % LS, which agrees the previous study on sodium activated slag systems [11] or the alkali-activated slag/fly ash systems [10]. However, the addition of high-volume (40 wt. %) LS coarsened the pore structure from nano-meter to micro-meter scale (**Figure 5a**). The pores are suspected to be the gaps between the unreacted limestone particles which resulted from the reduction of GGBS and the increase of the 'effective' w/b ratio. In other words, the hydration products (C-A-S-H gel) cannot sufficiently fill the gaps between these particles and the redundant alkaline solution will leave more pores after evaporation. By looking more specifically at the pore diameter ranges of the selected mixtures, it can be found that the pores that smaller than 15 nm were refined by the addition of less than 25 wt. % LS, whilst the pores within the same range in 40LS/60AAS pastes also increased dramatically. It is well known that the so-called 'gel pore' that in the range of 0.5 nm to 10 nm show significantly effect on the shrinkage [11, 28], while the drying shrinkage of 40LS/60AAS still less than that of 25LS/75AAS mortar. This result suggests that the unreacted limestone particles exhibit the 'skeleton effect' in the pastes, which reduced the shrinkage. Furthermore, the drying shrinkage reduction of high-volume LS mortars should possibly be attributed to the less gel phase and more 'skeleton' phase in the matrix.

### 3.3.2 XRD analysis

The phase assemblage of cementitious materials shows significant effect on the macro properties of its hardened matrix [29]. In pure sodium silicate activated LS system [5], the formation of new phase primarily depended on the modulus of sodium silicate solution (i.e. $Na_2O/SiO_2$ molar ratio). For newly formed crystals, it is found that Portlandite ($Ca(OH)_2$) and Pirssonite ($CaNa_2(CO_3)_2(H_2O)_2$) participated when the sodium silicate of Ms=0 (i.e. NaOH solution) was used and Thermonatrite ($Na_2CO_3H_2O$) formed when the Ms=1.0. However, rarely new crystals were found in the samples that activated by the sodium silicate solution with Ms=1.5. It is understandable that the available Ca ions are so easy to be combined with silicate anionic group to form C-S-H gel, which was further proved by the $^{29}Si$ MASNMR results [5]. The existing results are helpful for understanding the results in current study.

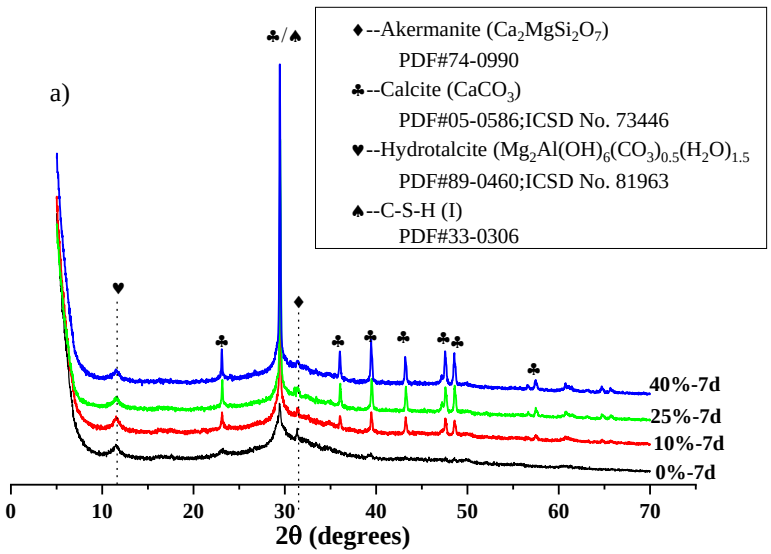
a)
♦--Akermanite ($Ca_2MgSi_2O_7$)
PDF#74-0990
♣--Calcite ($CaCO_3$)
PDF#05-0586;ICSD No. 73446
♥--Hydrotalcite ($Mg_2Al(OH)_6(CO_3)_{0.5}(H_2O)_{1.5}$
PDF#89-0460;ICSD No. 81963
♠--C-S-H (I)
PDF#33-0306
♣/♠
♥
♦
♣
40%-7d
25%-7d
10%-7d
0%-7d
0 10 20 30 40 50 60 70
2θ (degrees)

251

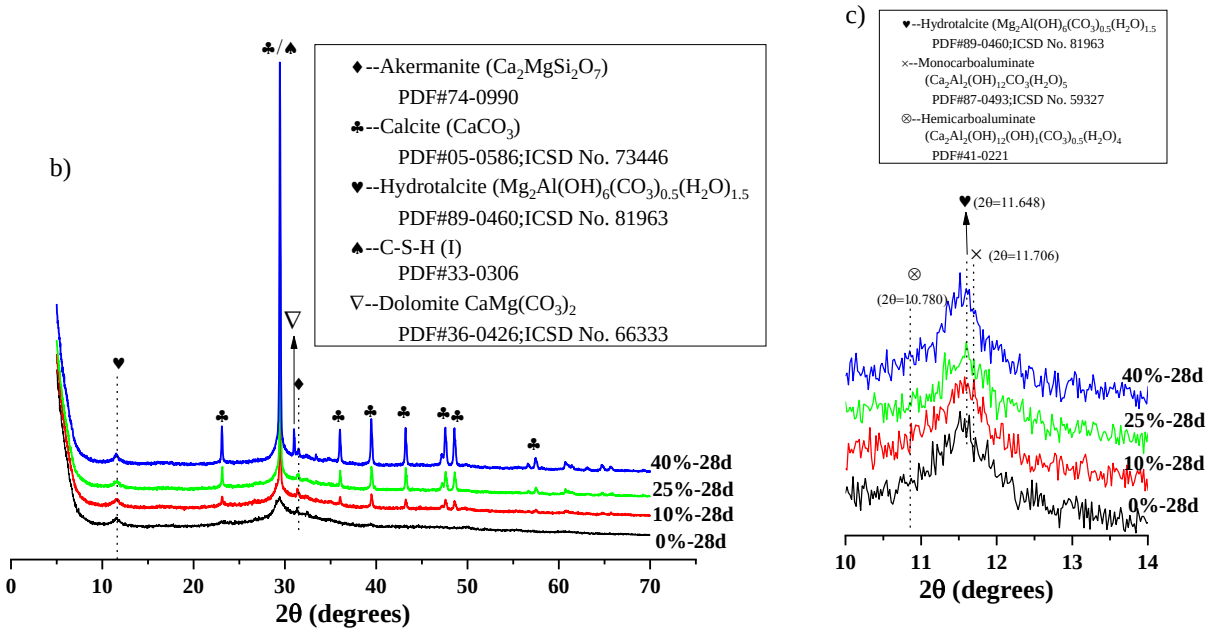
b)
♦--Akermanite ($Ca_2MgSi_2O_7$)
PDF#74-0990
♣--Calcite ($CaCO_3$)
PDF#05-0586;ICSD No. 73446
♥--Hydrotalcite ($Mg_2Al(OH)_6(CO_3)_{0.5}(H_2O)_{1.5}$
PDF#89-0460;ICSD No. 81963
♠--C-S-H (I)
PDF#33-0306
∇--Dolomite $CaMg(CO_3)_2$
PDF#36-0426;ICSD No. 66333
♣/♠
∇
40%-28d
25%-28d
10%-28d
0%-28d
0 10 20 30 40 50 60 70
2θ (degrees)
c)
♥--Hydrotalcite ($Mg_2Al(OH)_6(CO_3)_{0.5}(H_2O)_{1.5}$
PDF#89-0460;ICSD No. 81963
×--Monocarboaluminate
($Ca_2Al_2(OH)_{12}CO_3(H_2O)_5$
PDF#87-0493;ICSD No. 59327
⊗--Hemicarboaluminate
($Ca_2Al_2(OH)_{12}(OH)_1(CO_3)_{0.5}(H_2O)_4$
PDF#41-0221
♥(2θ=11.648)
×(2θ=11.706)
⊗
(2θ=10.780)
40%-28d
25%-28d
10%-28d
0%-28d
10 11 12 13 14
2θ (degrees)

252

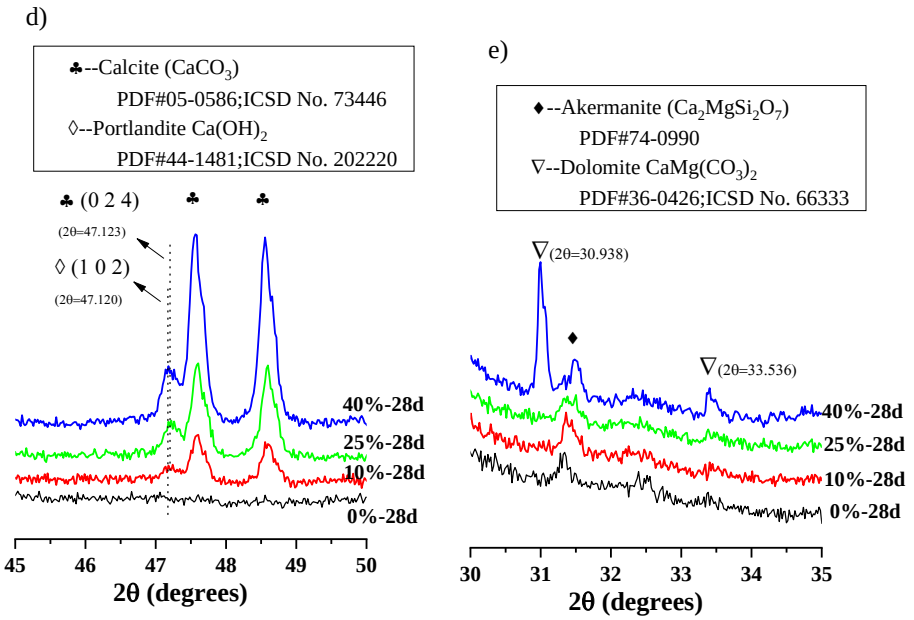


**Figure 6** XRD patterns of LS-AAS composites at (a) 7d; (b) 28d; (c) a close look at the calcium aluminate carbonates peaks, amplification of (b); (d) a closer look at the peak of (1 0 2) crystal face of Portlandite, amplification of (b); (e) a closer look at the peak of dolomite, amplification of (b).

**Figure 6a** and **6b** shows the XRD patterns of LS/AAS pastes (7 d and 28 d) that contain 10 wt. %, 25 wt. %, and 40 wt.% LS. Clearly, the major peaks in pure AAS pastes are assigned to C-S-H (I) (PDF #33-0306), and Mg-Al LDHs phase (PDF #89-0460) [30]. A small peak that belongs to the Akermanite (PDF #74-0990) were from the raw GGBS, which was gradually reduced as the loading of LS. In all LS/AAS pastes, the calcite (PDF #05-0586) peaks dominate the XRD patterns regardless of hydration age, indicating significant amount of LS remained in the system. Meanwhile, the C-S-H(I) and Mg-Al LDHs phase were still detectable in all samples. No obvious new peaks that can be assigned to new (crystal or amorphous) phases except a small Dolomite (PDF #36-0426) peak (**Figure 6b**) can be observed in pastes hydrated up to 28 d. This is reasonable since the sodium silicate solution used in this study has a Ms=1.2, which provides enough silicate groups that can be used to form C-S-H gel as discussed above.

By looking closer to the 28 d XRD patterns (**Figure 6b**) of LS/AAS pastes, the low-angle (**Figure 6c**), high-angle (**Figure 6d**), and median-angle (**Figure 6e**) features are enlarged and compared to some closely related phases. The (Hemi/Mono) carbon-aluminate phases (#PDF87-0493 & #PDF41-0221) that normally formed in LS added Portland cements [31] are specifically compared (**Figure 6c**). It is no doubt that the hemicarboaluminate was not present in the system. For the monocarboaluminate phase, the addition of LS did not significantly change the corresponding peak, which means the absence of such a phase in LS/AAS pastes. Therefore, the Al-phase in AAS preferred to form Mg-Al LDHs phase regardless of the presence of LS. It should be noticed that the Mg-Al LDHs phase can also bear some carbonates. For the shoulder peak that close to the main calcite peak (**Figure 6d**), which was indistinct for Portlandite (0 1 2) and calcite (0 2 4) crystal faces. One fact was that this shoulder peak increased simultaneously with the main calcite peak, indicating this ambiguous peak still belongs to calcite. By combining the previous study, it can be concluded that the portlandite was not present in LS/AAS pastes when the activator has a Ms>1.0. Surprisingly, the Dolomite peaks appeared in 40LS/60AAS samples (**Figure 6e**), whilst they were absence in samples that had LS contents less than 25 wt. %. There is no doubt that the Mg source can from either glassy phase or Akermanite phase (the corresponding peak was also changed in the same sample) in GGBS.

### 3.3.3 TG-DSC analysis

The LS contents in the LS/AAS pastes are quantitatively calculated using TG-DSC curves with tangent method [31]. **Figure 7a-7d** plot the TG-DSC changes of LS/AAS pastes hydrated for 7 d and 28 d respectively. The decomposition-temperature ranges of common phases [32], which are present in blended cements, namely C-S-H gel, AFt, AFm, CH (Portlandite), and $CaCO_3$, are given as the references for the LS/AAS composites. Two major peaks that associated to the mass loss of water from C-A-S-H (< 250 °C) and the mass loss of $CO_2$ from $CaCO_3$ (i. e. LS, 600 °C ~ 800 °C) can be observed in all samples except the reference paste. Only small (almost is not detectable, <1% as shown in **Figure 7e**) content of carbonates were found in reference group which was subtracted in the following calculation. The $CaCO_3$ residue content was calculated

according to **Equation 1**:

$$CaCO_{3\,residue}(\%) = CC\,\% \times \frac{molar\ mass\ of\ CaCO_3}{molar\ mass\ of\ CO_2} - CaCO_{3\,ref.}(\%) \quad \text{Equation 1}$$

where, the $CaCO_{3\ residue}$ is the residual $CaCO_3$ content in the LS/AAS pastes after hydration, which is given in **Figure 7e**. The CC% is the mass loss of $CO_2$ in the TG-DSC curves of each group. The $CaCO_{3ref}$ is the carbonates in neat AAS pastes that assumed to be due to carbonation, which is also given in **Figure 7e** (i.e. 0% LS group) but subtracted in the following groups. Normally, the calculated $CaCO_3$ content should be rescaled to the residual mass at 1000 ºC (i.e. the 'ignited weight'), however, the $CaCO_3$ content in pure LS powder using **Equation 1** was also used as the reference (**Figure 7f**) in this study. Therefore, the LS content can be rescaled (**Equation 2**) using the $CaCO_3$ content ($CaCO_{3LS}$ %) in pure LS, which should be closer to the original LS contents in the mixtures.

$$Rescaled\ LS\ content\ (\%) = \frac{CaCO_{3\ residue}(\%)}{CaCO_{3\ LS}(\%)} \quad \text{Equation 2}$$

where the rescaled LS content (**Figure 7g**) was used to compared to the corresponding replacement ratios of LS in each group. The estimated hydration degree of LS is thus given in **Figure 7h**.

The general trend of the hydration degree of LS also follows those of mechanical and drying shrinkage properties. Other interesting results can be found that: i) at lower replacement content (10 wt.%), the hydration degree of LS did not increase from 7 d to 28 d; ii) at medium replacement ratio (25 wt. %), the hydration degree slightly increased (~ 2%) and ; iii) at high replacement ratio (40 wt. %), the hydration degree continuously increased at the same hydration time range (~ 12%). The highest hydration degree of LS happened at the replacement ratio of 25 wt. %, this evidence supported the highest mechanical strengths and drying shrinkage were achieved by 25LS/75AAS composites.

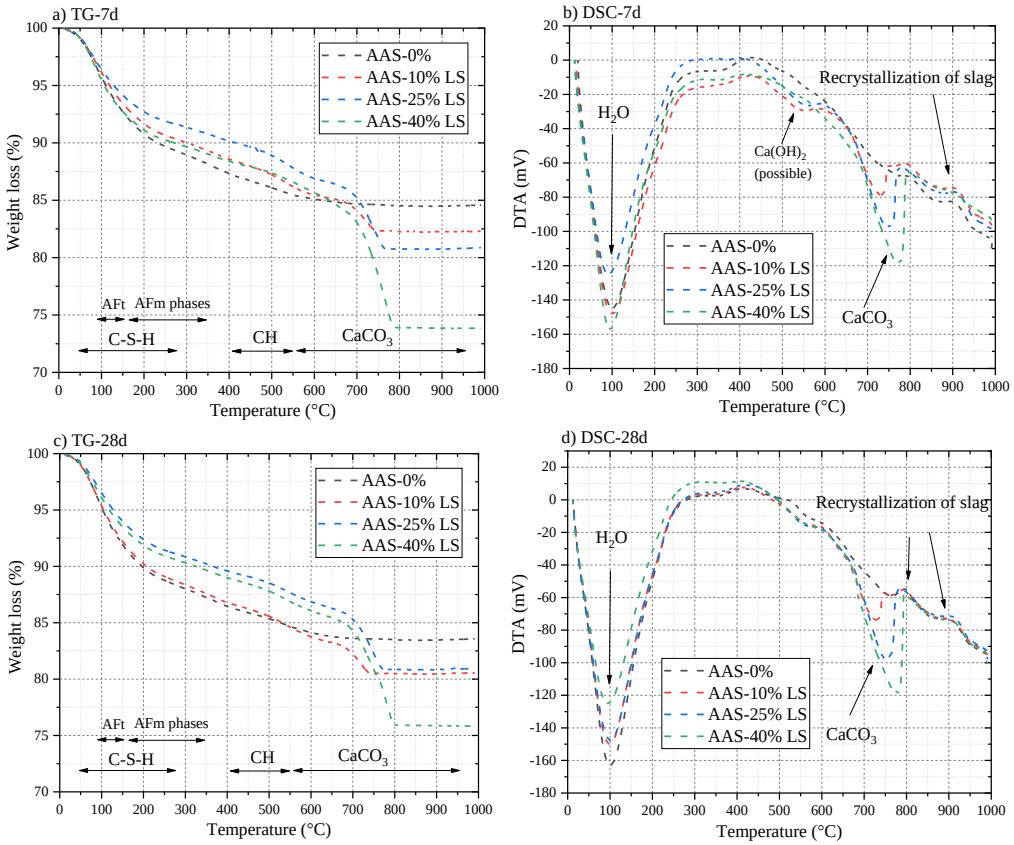

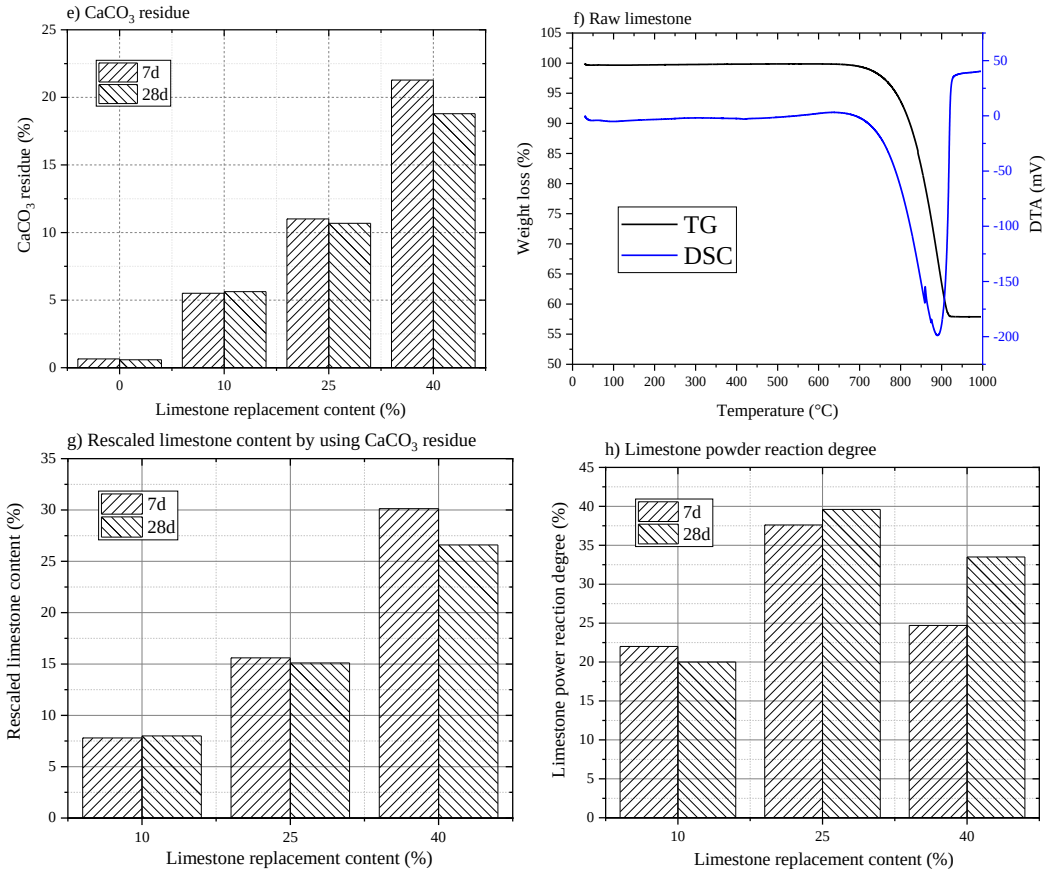


**Figure 7** TG-DSC curves of LS-AAS composites at (a)-(b): 7 d; (c)-(d) 28 d; (e) residual $CaCO_3$ content calculated from (a)~(d); (f) TG-DSC curves of raw limestone for the calibration of $CaCO_3$ content; (g) rescaled of $CaCO_3$ content with the result of (f); (h) calculated hydration degree of LS powder in each systems.

### 3.3.4 FTIR analysis

**Figure 8a** gives the FTIR spectra of the LS/AAS pastes at 28 d and the spectrum of raw LS is given in **Figure 8b** as the reference. In the neat paste, the major bands on the spectrum are assigned to the vibration of O-H bonds in water at ~3400 $cm^{-1}$ or ~1600 $cm^{-1}$ and the $\nu_3$(Si-O) bonds in C-A-S-H gel phase at ~980 $cm^{-1}$ [33]. Small bands at ~860 $cm^{-1}$ or ~1420 $cm^{-1}$ that related to the C-O vibrations show that trace carbonation happened during testing [33]. For the FTIR spectrum of the raw LS (**Figure 8b**), three major peaks that corresponding to the C-O vibrations are the main IR bands of LS. One significant feature is that the $\nu_4$(C-O) at ~ 740 $cm^{-1}$ raw LS [34] is more obvious when compared to the same position in neat AAS spectrum. In addition, the band of bridging carbonates at ~ 1760 $cm^{-1}$ can be found in raw LS [34], which cannot be detected in neat AAS paste. These features can be used as the trackers for the presence of raw LS in the LS/AAS pastes.

Comparing the FTIR spectra of LS/AAS pastes with that of the pure AAS paste, the two featured bands (i. e. $\nu_4$(C-O) at ~ 740 $cm^{-1}$ and bridging carbonates at ~ 1760 $cm^{-1}$) were detected in all LS/AAS pastes, indicating the residual raw LS were present in the pastes hydrated for 28 d. Two major peaks (~860 $cm^{-1}$ or ~1420 $cm^{-1}$) of C-O vibrations were found in all LS-added samples and these peaks became more distinct as the increased loading of LS. The vibration bond that related to C-A-S-H at ~980 $cm^{-1}$ was detected in all samples, indicating that the major binding phase in all samples remained unchanged.

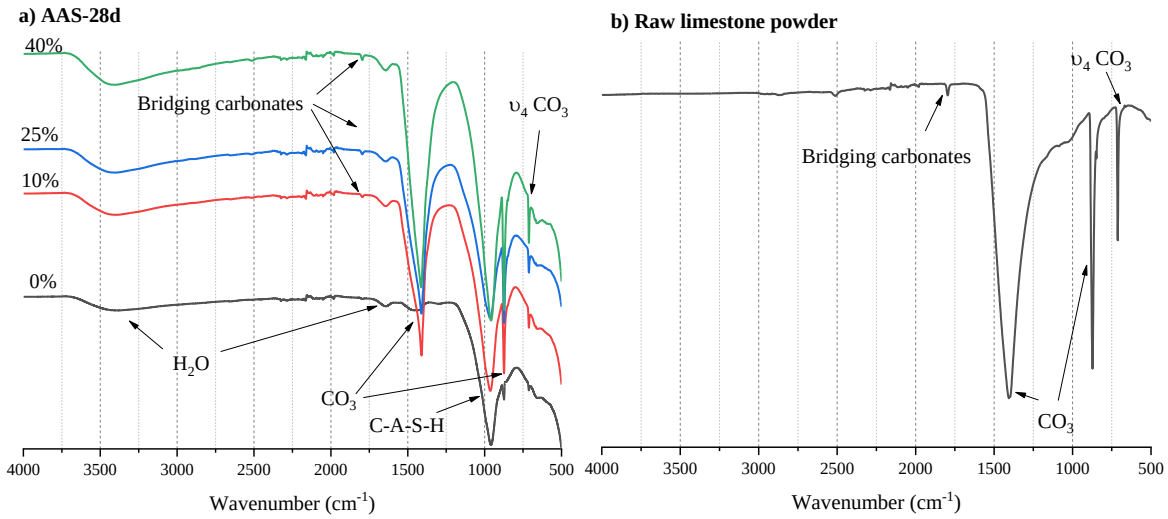


Figure 8 FTIR spectra of: (a) LS-AAS composites at 28d and (b) raw LS powder.

### 3.3.5 SEM/EDS analysis

**Figure 9** shows the SEM observations of fracture surfaces of 40LS/60AAS pastes hydrated for 28 d at the magnification of 5.0 k and 10.0 k. Two featured micro-morphologies, one area of well-dispersed LS (**Figure 9a**) and one of agminated LS (**Figure 9b**), are shown at micro-meter level. The reacted LS particles (marked as 'r') with cubic morphology was found to closely adhere to the AAS matrix. The reacted particles also showed the features of deep colour that was close to the surrounded C-S-H gel. An area of agminated LS particles was found in high-volume LS/AAS pastes as shown in **Figure 9b**. Two distinct features with light and deep colours were observed, suggesting some unreacted LS particles may be found in the agminated LS regions. This finding suggests that the proper dispersion of LS particles is essential for the improvement of its hydration degree.

**Figure 10** was further used for EDX mapping analysis of Na, Al, Si, and Ca element distributions for the area included both deep and light colours LS particles. The Ca distributed around the analysed area, indicating that these features should be the LS particles. One interesting feature is that the Na tended to be present in the dark-colour regions, indicating that this area might be covered by C-A-S-H phase since the Na ions preferred to be adsorbed by the negative-charged gel (i. e. C-A-S-H gel) [35], thus confirming the reaction of LS happened in AAS system.

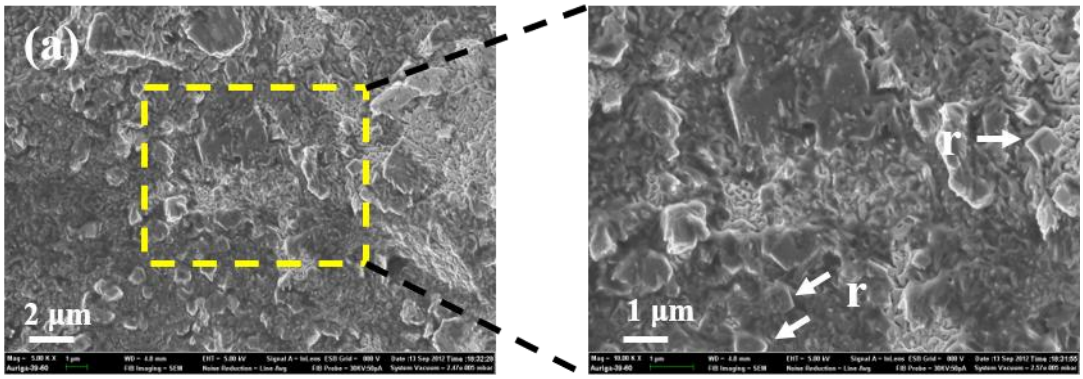

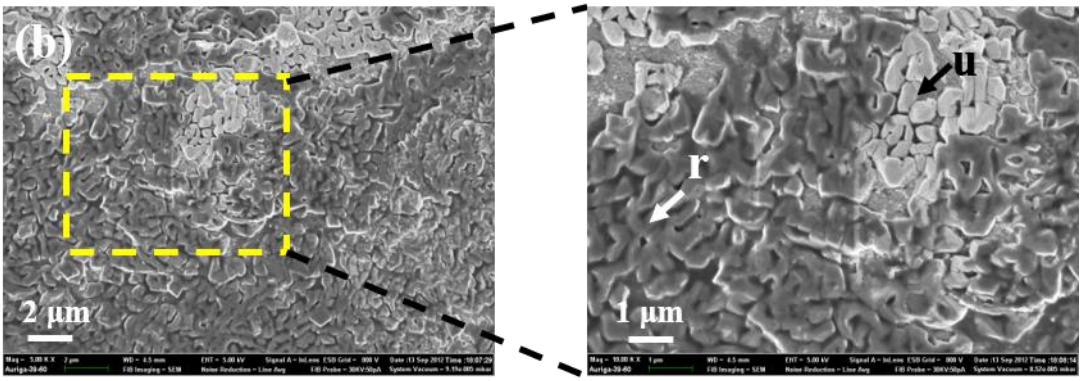


**Figure 9** SEM observations of 40LS/60AAS composites: (a) an area of well-dispersed LS with the observed magnifications at ×5.0 k and ×10.0 k; (b) an area of agminated LS with the observed magnifications of ×5.0 k and ×10.0 k. The reacted LS particles are labelled with 'r' and the unreacted LS particles are labelled with 'u'.

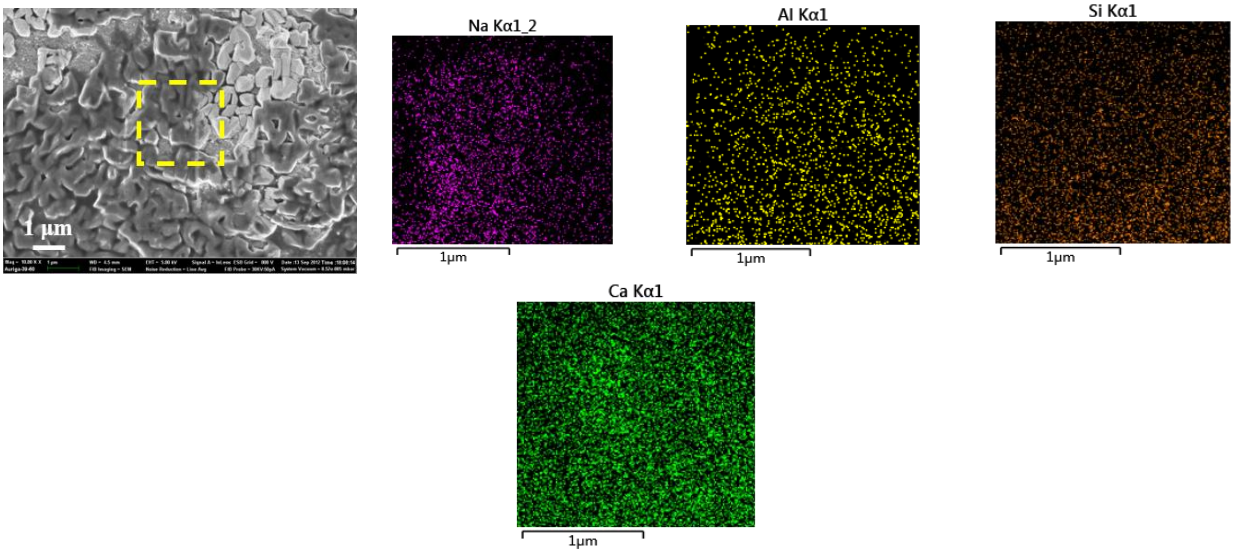


**Figure 10** SEM-EDX Mapping of the selected area that contains both reacted and unreacted LS particles shows the elements distribution of Na, Al, Si, and Ca.

# 4. Summary and conclusions

The properties of 0 ~ 50 wt. % limestone powder (LS) modified AAS composites were explored in this study. The physical effect (pore structure change) of LS in AAS system was studied by $N_2$- adsorption test, whist the chemical effects were investigated through XRD, TG-DSC, FTIR, and SEM/EDX analyses. The major findings can be summarised as follows:

1. The increased fluidity and prolonged setting time of AAS pastes were achieved by using LS, whilst the highest compressive and flexural strengths were found in the mortars with 25 wt. % LS incorporated.
2. The drying shrinkage showed the same tendency as the mechanical properties of LS/AAS mortars with the highest shrinkage values were given by 25 wt. % LS replaced samples.
3. The pore structure was refined by replacing up to 25 wt. % LS, but was hugely coarsened by using 40 wt. % LS.
4. In regarding to new hydration products due the addition of LS, only small amount of dolomite was confirmed in 40 wt. % LS replaced pastes. The hydration products of LS/AAS pastes is believed to be affected by the modulus (Ms) of sodium silicate solution. The C-S-H gel should be the main hydration products when Ms > 1.0.
5. The highest hydration degree of LS was also found in 25 wt. % LS replaced pastes. For high-volume replaced samples (40 wt. %), around 30 ~ 35 % hydration degree of LS was achieved within 28 d of hydration.
6. The agminated LS regions were found in high-volume LS replaced sample by SEM-EDX, suggesting that the proper dispersion of LS particles is essential for improving its hydration degree.

# Acknowledgements

The experiments were carried out at Chongqing University and Harbin Institute of Technology (Supported by

Shouheng Jiang). This project was supported by the SRTP (Student Research Training Programme) of Chongqing University (CQU-SRTP-2014175). The supports from NSFC (NO. 51878102) and University of Leeds during the preparation of manuscript are also appreciated.

# References

1. Cancio Díaz, Y., S. Sánchez Berriel, U. Heierli, A. R. Favier, I. R. Sánchez Machado, K. L. Scrivener, J. F. Martirena Hernández and G. Habert (2017). "Limestone calcined clay cement as a low-carbon solution to meet expanding cement demand in emerging economies." Development Engineering **2**: 82-91.
2. Juenger, M. C. G., F. Winnefeld, J. L. Provis and J. H. Ideker (2011). "Advances in alternative cementitious binders." Cement and Concrete Research **41**(12): 1232-1243.
3. Moseson, A. J., Moseson, D. E., & Barsoum, M. W. (2012). High volume limestone alkali-activated cement developed by design of experiment. Cement and Concrete Composites, **34**(3), 328-336.
4. Bernal, S. A., J. L. Provis and D. J. Green (2014). "Durability of Alkali-Activated Materials: Progress and Perspectives." Journal of the American Ceramic Society **97**(4): 997-1008.
5. Ortega-Zavala, D. E., J. L. Santana-Carrillo, O. Burciaga-Díaz and J. I. Escalante-García (2019). "An initial study on alkali activated limestone binders." Cement and Concrete Research **120**: 267-278.
6. Wang, D., et al., A review on use of limestone powder in cement-based materials: Mechanism, hydration and microstructures. Construction and Building Materials, 2018. 181: p. 659-672.
7. Li, C. and L. Jiang, Utilization of limestone powder as an activator for early-age strength improvement of slag concrete. Construction and Building Materials, 2020. 253: p. 119257.
8. Menchaca-Ballinas, L.E. and J.I. Escalante-García, Limestone as aggregate and precursor in binders of waste glass activated by CaO and NaOH. Construction and Building Materials, 2020. 262: p. 120013.
9. Adewumi, A.A., et al., Effect of sodium hydroxide concentration on strength and microstructure of alkali-activated natural pozzolan and limestone powder mortar. Construction and Building Materials, 2021. 271: p. 121530.
10. Xiang, J., et al., Effect of limestone on rheological, shrinkage and mechanical properties of alkali – Activated slag/fly ash grouting materials. Construction and Building Materials, 2018. 191: p. 1285-1292.
11. Yuan, B., et al., Autogenous and drying shrinkage of sodium carbonate activated slag altered by limestone powder incorporation. Construction and Building Materials, 2017. 153: p. 459-468.
12. Rakhimova, N. R., & Rakhimov, R. Z. (2014). A review on alkali-activated slag cements incorporated with supplementary materials. Journal of Sustainable Cement-Based Materials, **3**(1), 61-74.
13. Zhu, X., D. Tang, K. Yang, Z. Zhang, Q. Li, Q. Pan and C. Yang (2018). "Effect of $Ca(OH)_2$ on shrinkage characteristics and microstructures of alkali-activated slag concrete." Construction and Building Materials **175**: 467-482.
14. Luo, Y., C. Wang, C. Luo, Q. Huang, S. Wang and X. Peng (2016). "Effect of electrical field on TSA failure of cement-based materials." Cement and Concrete Research **90**(12): 19-26.
15. Zhu, X., Z. Zhang, K. Yang, B. Magee, Y. Wang, L. Yu, S. Nanukuttan, Q. Li, S. Mu, C. Yang and M. Basheer (2018). "Characterisation of pore structure development of alkali-activated slag cement during early hydration using electrical responses." Cement and Concrete Composites **89**: 139-149.
16. Jin, F., K. Gu and A. Al-Tabbaa (2014). "Strength and drying shrinkage of reactive MgO modified alkali-activated slag paste." Construction and Building Materials **51**: 395-404.
17. Bayiha, B. N., N. Billong, E. Yamb, R. C. Kaze and R. Nzengwa (2019). "Effect of limestone dosages on some properties of geopolymer from thermally activated halloysite." Construction and Building Materials 217: 28-35.
18. Zhu, X., M. Zhang, Y. Yang, K. Yang, F. Wu, Q. Li, L. Yu, C. Yang and M. Basheer (2019). "Understanding the aqueous phase of alkali-activated slag paste under bath-curing." Advances in Cement Research: 1-33.
19. Cwirzen, A., J. L. Provis, V. Penttala and K. Habermehl-Cwirzen (2014). "The effect of limestone on sodium hydroxide-activated metakaolin-based geopolymers." Construction and Building Materials **66**: 53-62.
20. Rakhimova, N. R., R. Z. Rakhimov, N. I. Naumkina, A. F. Khuzin and Y. N. Osin (2016). "Influence of limestone content, fineness, and composition on the properties and microstructure of alkali-activated slag cement." Cement and Concrete Composites **72**: 268-274.
21. Li, J., Zhang, W., Xu, K., & Monteiro, P. J. (2020). Fibrillar calcium silicate hydrate seeds from hydrated tricalcium silicate lower cement demand. Cement and Concrete Research, **137**, 106195.
22. Ye, H. and A. Radlińska (2017). "Shrinkage mitigation strategies in alkali-activated slag." Cement and

Concrete Research **101**: 131-143.
23. Sakulich, A. R. and D. P. Bentz (2012). "Mitigation of autogenous shrinkage in alkali activated slag mortars by internal curing." Materials and Structures **46**(8): 1355-1367.
24. Ye, H., C. Cartwright, F. Rajabipour and A. Radlińska (2017). "Understanding the drying shrinkage performance of alkali-activated slag mortars." Cement and Concrete Composites **76**: 13-24.
25. Ye, H. and A. Radlińska (2016). "Shrinkage mechanisms of alkali-activated slag." Cement and Concrete Research **88**: 126-135.
26. Cai, Y., L. Yu, Y. Yang, Y. Gao and C. Yang (2019). "Effect of Early Age-Curing Methods on Drying Shrinkage of Alkali-Activated Slag Concrete." Materials **12**(10): 1633.
27. Zhang, B. (1998). "Relationship between pore structure and mechanical properties of ordinary concrete under bending fatigue." Cement and concrete research **28**(5): 699-711.
28. Collins, F. and J. G. Sanjayan (2001). "Microcracking and strength development of alkali activated slag concrete." Cement and Concrete Composites **23**: 345-352.
29. Richardson, I. G. (2000). "The nature of the hydration products in hardened cements." Cement and Concrete Composites **22**: 97-113.
30. Zhu, X. H., X. J. Kang, K. Yang and C. H. Yang (2017). "Effect of graphene oxide on the mechanical properties and the formation of layered double hydroxides (LDHs) in alkali-activated slag cement." Construction and Building Materials **132**: 290-295.
31. Adu-Amankwah, S., M. Zajac, C. Stabler, B. Lothenbach and L. Black (2017). "Influence of limestone on the hydration of ternary slag cements." Cement and Concrete Research **100**: 96-109.
32. Alarcon-Ruiz, L., G. Platret, E. Massieu and A. Ehrlacher (2005). "The use of thermal analysis in assessing the effect of temperature on a cement paste." Cement and Concrete Research **35**(3): 609-613.
33. Trevor L. Hughes, Claire M. Methven, Timothy G.J. Jones, Sarah E. Pelham, Philip Fletcher and C. Hall (1995). "Determining cement composition by Fourier Transform Infrared Spectroscoy." Advanced Cement Based Materials **2**: 91-104.
34. Philippi, R. and K. Fujimoto (1992). "FTIR spectroscopic study of carbon dioxide adsorption_desorption on magnesia_calcium oxide catalysts." J. Phys. Chem. **96**: 9035-9038.
35. Ye, H. (2018). "Nanoscale attraction between calcium-aluminosilicate-hydrate and Mg-Al layered double hydroxides in alkali-activated slag." Materials Characterization **140**: 95-102.